

# The Stability of Euclidean Wormholes

James Chryssanthacopoulos<sup>1</sup>

<sup>1</sup>University of Padova, Padova PD, Italy

jamespeter.chryssanthacopoulos@studenti.unipd.it

**Abstract.** *Wormholes are intriguing solutions to general relativity that connect distant asymptotic regions of spacetime. While many types of wormholes have been studied for decades, Euclidean wormholes have received renewed interest because of their role in showing how information can be recovered from a black hole. Another related issue that wormholes raise is the inability to factorize the gravitational path integral between two geometries if a wormhole connects them. In AdS/CFT, this implies that the bulk is dual to an ensemble of quantum field theories on the asymptotic boundaries, which defies the traditional understanding of the correspondence. This problem is only serious if the wormhole is stable, or free of negative modes. This report identifies wormhole solutions in a representative low-energy model inspired by string theory and analyzes its negative modes. Implications for the factorization problem are discussed.*

## 1. Introduction

In general relativity, the geometry of spacetime is a dynamic field that changes depending on the matter and energy it contains. Classical solutions to general relativity, wormholes are geometries that connect two asymptotic regions of spacetime [1]. Historically, wormholes arose in the context of black holes, but they can represent more general geometries. Whatever the kind of wormhole, they are generally not humanly traversable unless supported by some exotic matter field. Although they have been studied for decades, wormholes have received renewed interest because of their role in raising and resolving issues in quantum gravity.

One aspect of quantum gravity that wormholes complicate is the AdS/CFT correspondence. One of the most significant developments in quantum gravity in recent decades, the AdS/CFT correspondence is a concrete example of the holographic principle, which relates the physics in a volume of space to information encoded on its boundary. Specifically, the AdS/CFT correspondence establishes a connection between a gravitational system in asymptotically anti-de Sitter space and a conformal field theory defined on its boundary, depicted in Figure 1 [2]. The gravitational system is described by strings propagating in the bulk, which is equated to quantum fields propagating on the boundary. Formally, the correspondence equates the partition function of the conformal field theory on the boundary to the partition function of string theory in the bulk,

$$Z_{\text{CFT}}(h) = Z_S(h), \quad (1)$$

where  $h$  is the boundary metric [3]. At low energy, string theory can be approximated by classical supergravity, allowing  $Z_S$  to be computed by  $\exp(-S[g])$ , where  $S[g]$  is the action of the solution  $g$  of the Einstein equations with the given boundary condition. More generally,  $Z_S$  is the path integral over all metrics consistent with the boundary.

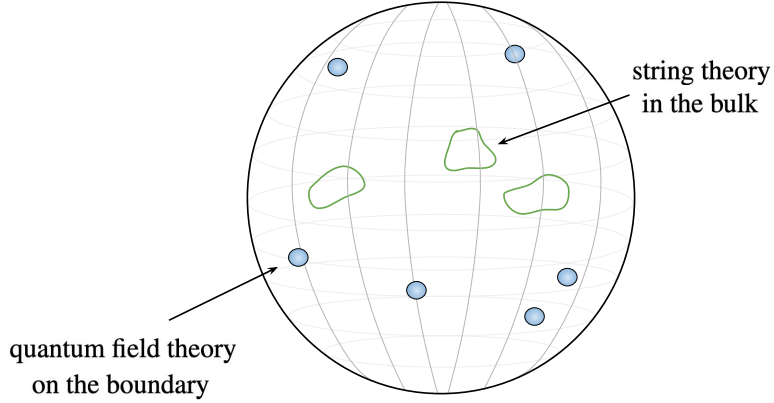


**Figure 1. The AdS/CFT correspondence relates string theory in asymptotically anti-de Sitter space to a conformal field theory on the boundary.**

A more general formulation of AdS/CFT involves the generating functional of correlation functions of operators in the conformal field theory, where the sources are the boundary values of bulk fields. For example, if  $\phi$  is a massless field in the bulk whose boundary value is  $\phi_0$ , then the correspondence says

$$\left\langle \exp \int_{\partial\mathcal{M}} \phi_0 \mathcal{O} \right\rangle = Z_S(\phi_0),$$

where  $\mathcal{O}$  is an operator on the boundary  $\partial\mathcal{M}$ . Correlation functions are generated by differentiating with respect to the boundary field, which acts as the source. Another example involves gauge fields  $A_a$  in the bulk, and associated currents  $J_a$  on the boundary,

$$\left\langle \exp \int_{\partial\mathcal{M}} A_0^a J_a \right\rangle = Z_S(A_0).$$

Equation 1 is another example of this type of relation. Because  $T_{\mu\nu} = \delta S / \delta g^{\mu\nu}$ , differentiating the boundary partition function with respect to the metric generates correlation functions between stress tensors on the boundary.

One important application of these relations is that they permit correlation functions of potentially strongly coupled quantum field theories to be computed using solutions to weakly coupled gravitational systems. For example, the most important example of the AdS/CFT correspondence equates  $\mathcal{N} = 4$  super Yang-Mills theory in four dimensions, with gauge group  $SU(N)$ , to Type IIB superstring theory on  $\text{AdS}_5 \times S^5$ . In the large  $N$  limit, the string theory is weakly coupled and can be approximated by tree-level supergravity. This allows correlation functions of strongly coupled super Yang-Mills theory to be computed more easily than they otherwise would. Beyond this increased computational power, AdS/CFT provides a concrete relation between gravitational and quantum systems, hinting at a possible way the fabric of spacetime may emerge from the entanglement between quantum fields.

In the traditional understanding of AdS/CFT, the path integral  $Z_S$  is taken over configurations that have a single compact boundary. To extend AdS/CFT to account for

wormholes, which have multiple boundaries, the gravitational theory can be equated naturally to several quantum field theories over different boundaries. This potentially conflicts with existing evidence that suggests that string theory is dual to a single quantum field theory on the boundary. If there really is a duality with multiple quantum field theories, the presence of the wormhole implies a correlation between them that AdS/CFT does not account for [4].

A closely related issue that wormholes raise concerns the ability to factor path integrals over geometries with multiple boundaries, depicted in Figure 2. Let  $\langle Z \rangle$  be the path integral over all geometries terminating in a single boundary. When there are two boundaries, the path integral  $\langle Z^2 \rangle$  should be the product of those for two disconnected geometries,  $\langle Z \rangle^2$ . The wormhole connecting the boundaries adds a contribution to the path integral that violates this factorization. In the context of AdS/CFT, this inability to factor the path integral introduces correlations between observables on the two boundaries in the gravitational theory, which implies the presence of correlations between the corresponding quantum field theories.

$$\begin{aligned} \langle Z \rangle &= \text{[Diagram of a single cone-like geometry with one boundary]} \\ \langle Z^2 \rangle &= \left( \text{[Diagram of two disconnected cone-like geometries]} \right) + \text{[Diagram of a wormhole connecting two boundaries]} \\ &\neq \langle Z \rangle^2 \end{aligned}$$

**Figure 2. The path integral over all geometries with two boundaries does not factorize if a wormhole connects the boundaries. This figure is adapted from [5].**

While wormholes challenge the traditional understanding of AdS/CFT, it is unclear the extent to which wormhole solutions contribute to the full calculation of the path integral. The path integral over all geometries is given by

$$Z = \int \mathcal{D}g e^{iS[g]},$$

where  $g$  is the metric tensor and  $S[g]$  is the action functional for a given metric. Since the exponential is an oscillating function, it is common to perform a Wick rotation, introducing the Euclidean time,  $t = -i\tau$ . The path integral becomes

$$Z = \int \mathcal{D}g e^{-S[g]}.$$

Although the integral is performed over all metrics consistent with the boundary conditions, the presence of the minus sign in the exponential means that the integral is dominated by metrics that minimize the action, as shown in Figure 3. Wormholes are given by metrics that are usually found by solving the Einstein equations, but those solutions

extremize the action, not necessarily minimize it. If a wormhole solution maximizes the action, it may not contribute significantly to the overall path integral. In that case, its role in the problems just described may be limited.

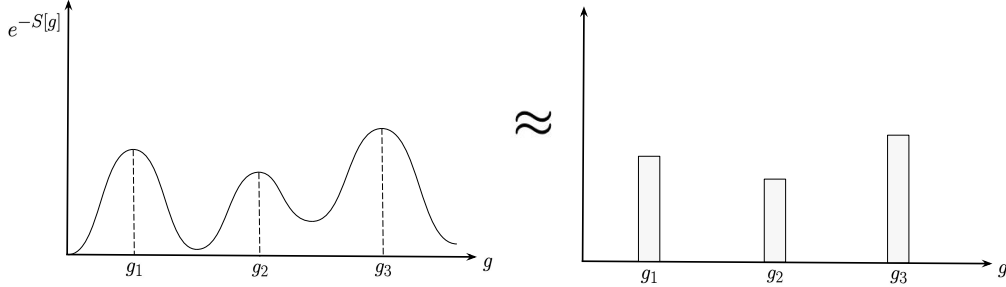


**Figure 3.** The gravitational path integral is the sum over all geometries, but if the configuration space is dominated by a few points with low action, the path integral can be approximated by the sum over only those metrics.

Wormholes that arise from extremizing the action in Euclidean signature are called Euclidean wormholes. Unlike wormholes in Lorentzian signature, they do not necessarily correspond to wormholes that exist in the universe, which is described by a Lorentzian metric. Instead, they represent more formal and technical solutions that may dominate the gravitational path integral. One way of determining whether a wormhole is dominant is by checking if it is unstable when perturbed [6]. This involves expressing the action in terms of fluctuations of the metric around the wormhole solution and checking if it has negative eigenvalues. These negative modes are not expected to dominate when integrated over nearby configurations in the path integral. In this way, understanding negative modes is crucial in assessing the importance of wormholes in quantum gravity.

One major reason why wormholes are important in quantum gravity is because they help to explain how information is recovered from a black hole. According to general relativity, anything that falls into a black hole cannot be recovered, but this conflicts with quantum mechanics, which conserves information. Combining general relativity and quantum mechanics semiclassically, it was shown that a black hole emits radiation, as shown in Figure 4. At the event horizon, one particle in a particle-antiparticle pair formed from the vacuum falls into the black hole, while the other is emitted. If the infalling particle is trapped inside the black hole, the entropy of the emitted radiation continuously increases. Since the AdS/CFT correspondence regards a black hole as a quantum system, information should be conserved and the entropy should eventually decrease. This evolution of entropy that increases, then decreases, is known as the Page curve, depicted in Figure 5 [7]. Wormholes are needed to reproduce the entanglement entropy of radiation given by the Page curve.

The entropy is calculated using holography. As already mentioned, holography establishes a connection between correlation functions of operators on the boundary and fields in the bulk, but another example of the holographic mapping involves quantum information. One measure of quantum information of a boundary region  $A$  is the von Neumann entropy

$$S_A = -\text{Tr}(\rho_A \log \rho_A),$$

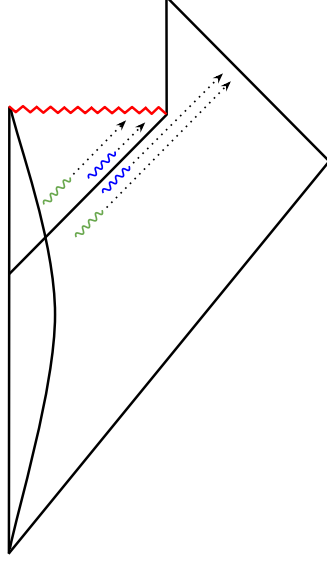


**Figure 4. A black hole formed from collapsing matter emits radiation at the event horizon. One particle escapes to asymptotically Minkowski space, while the other falls into the black hole. This figure is adapted from [8].**

where  $\rho_A$  is the reduced density matrix of the region computed by tracing over the degrees of freedom outside of  $A$ ,  $\rho_A = \text{Tr}_{\bar{A}}(\rho)$ . On the gravitational side, the entropy can be computed using the Ryu-Takayanagi formula [9]

$$S_A = \frac{\text{Area}(\gamma_A)}{4G_N},$$

where  $\gamma_A$  is the codimension-two hypersurface in the bulk with minimal area that shares the same boundary as  $A$ , among other requirements. This geometry is depicted schematically in Figure 6.

When applied to black hole radiation, the Ryu-Takayanagi formula does not compute the entropy of the radiation, but reflects the entropy of the overall gravitational system that contains a black hole. In this way, it is a generalization of the black hole entropy in terms of the area of the event horizon [10]. To account for the quantum effects of radiation in the bulk, an additional contribution needs to be added,

$$S_A = \min \left[ \frac{\text{Area}(\gamma_A)}{4G_N} + S_{\text{bulk}} \right],$$

where  $S_{\text{bulk}}$  is the entanglement of the radiation induced by the presence of the surface  $\gamma_A$ . The minimization is carried out over all possible surfaces satisfying the constraints.

While the quantum-corrected Ryu-Takayanagi formula incorporates the entropy of matter fields, it is insufficient to model the entropy of radiation during black hole evaporation. This is because as the black hole shrinks, at some point the entropy of the radiation should decrease, but  $S_{\text{bulk}}$  continues to grow. To account for entanglement with radiation in the black hole interior, the entropy is given by

$$S_{\text{rad}} = \min_X \left\{ \text{ext}_X \left[ \frac{\text{Area}(X)}{4G_N} + S_{\text{sc}}(\Sigma_{\text{rad}} \cup \Sigma_{\text{island}}) \right] \right\}, \quad (2)$$

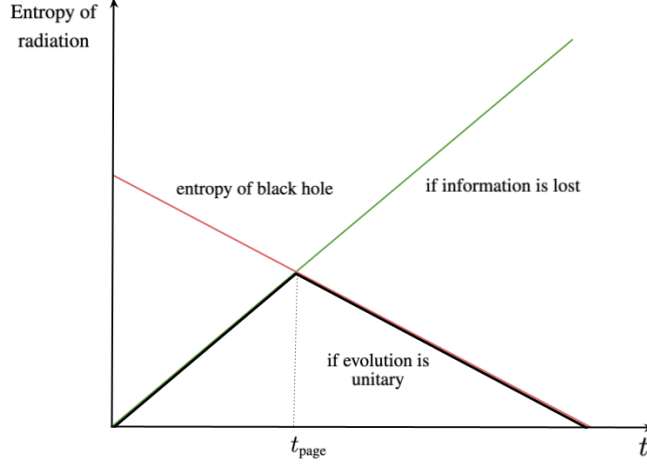


**Figure 5.** If information is recovered during evaporation, the entropy of black hole radiation initially increases, then starts to decrease when the entropy equals that of the black hole. If information is lost inside the black hole, the radiation entropy will continue to increase.

where the extremization is performed over a general surface  $X$  [11]. The semiclassical entropy  $S_{\text{sc}}$  is computed over the union of two disconnected regions, shown in Figure 7. The region  $\Sigma_{\text{rad}}$  encompasses the area from a given cutoff surface to the exterior boundary, while  $\Sigma_{\text{island}}$  encompasses the region from the surface  $X$  to the interior boundary. As the black hole continues to evaporate,  $\Sigma_{\text{island}}$  grows, allowing the entropy to decrease. Intuitively, the center of the black hole becomes identified with the outgoing radiation, although it is separated across the event horizon.

To derive the island formula of Equation 2, wormholes play a crucial role. The semiclassical entropy of the radiation can be computed from its density matrix prepared using the gravitational path integral. Specifically, if the initial state of radiation is given by the wavefunction  $|\Psi_i\rangle$ , the amplitude of transitioning to the final state  $|\Psi_f\rangle$  is given by the path integral

$$\langle \Psi_f | \Psi_i \rangle = \int_{g_i}^{g_f} \mathcal{D}g e^{-S[g]},$$

where  $g_i$  and  $g_f$  are the metrics corresponding to the geometries of the initial and final states, respectively. The elements of the density matrix are then

$$\rho_{ab} = \langle \Psi_a | \Psi_i \rangle \langle \Psi_i | \Psi_b \rangle.$$

From the density matrix, the entropy can be computed,

$$S = (1 - n \partial_n) \log \text{Tr}(\rho^n) \Big|_{n=1}.$$

This calculation can be viewed as replicating the system  $n$  times and summing over the different ways of connecting the black hole interior [12]. Consider the case where  $n = 2$ , which involves calculating  $\text{Tr}(\rho^2)$ , called the purity. This calculation is shown in Figure 8. The cigar geometry represents the density matrix in terms of two black holes glued together with exterior geometries  $g_a$  and  $g_b$ . To perform the calculation, different ways of

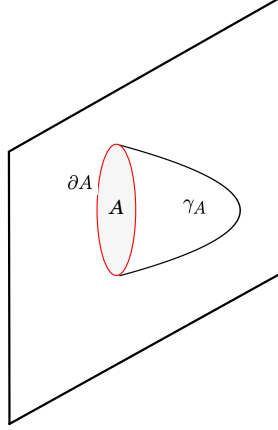


**Figure 6.** The entanglement entropy of quantum fields on  $A$  can be computed from the area of the codimension-two hypersurface in the bulk that shares the same boundary.

connecting the interiors need to be added. In the disconnected configuration, the entropy grows linearly in time. When the black holes are connected by a wormhole, the entropy is initially lower because the path integral incurs an extra factor of  $e^{-G}$ , where  $G$  is the genus of the wormhole. At later times, the disconnected configuration becomes heavily suppressed by the kinematics, allowing the wormhole to dominate. Because the presence of the wormhole makes the state of the radiation pure, it drives the entropy down to zero. This rising, then falling, behavior of the entropy captures the trend of Equation 2 and is due to the competition between disconnected and wormhole solutions.

While it is not immediately apparent, the calculation of black hole radiation actually manifests the same factorization problem of the path integral previously discussed. Without entering into all the details, this has been shown for the simple case of a black hole in two-dimensional Jackiw–Teitelboim gravity, with a so-called “end of the world brane” behind the horizon [13]. The brane has  $k$  states, which describe the interior partners of the early radiation. This brane is entangled with the early radiation of the black hole. Together, the state of the system is

$$|\Psi\rangle = \frac{1}{\sqrt{k}} \sum_{i=1}^k |\Psi_i\rangle_B |i\rangle_R,$$

where  $|\Psi_i\rangle_B$  is the state of the brane and  $|i\rangle_R$  is that of the radiation. Calculating the reduced density matrix of the radiation, and taking the trace, it can be shown that

$$\text{Tr}(\rho_R^2) = \frac{1}{k^2} \sum_{i,j=1}^k |\langle \Psi_i | \Psi_j \rangle|^2. \quad (3)$$

As Figure 8 demonstrated, calculating the purity involves adding disconnected and connected contributions. It turns out that the purity evaluates to

$$\text{Tr}(\rho_R^2) = \frac{1}{k} + \frac{Z_2}{Z_1^2}, \quad (4)$$

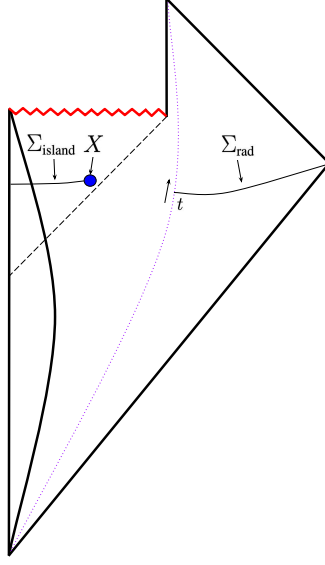


**Figure 7. To compute the radiation entropy, the area of the surface  $X$  is added to the semiclassical entropy over the union between regions both outside and inside the black hole. This figure is adapted from [8].**

where  $Z_1$  and  $Z_2$  are the actions of the disconnected solution and wormhole, respectively. Comparing Equation 4 with Equation 3, it follows that

$$|\langle \Psi_i | \Psi_j \rangle|^2 = \delta_{ij} + \frac{Z_2}{Z_1^2}.$$

Alternatively, since the brane consists of orthogonal states, it must be that  $\langle \Psi_i | \Psi_j \rangle = \delta_{ij}$ . The conflict between this and the previous equation is another manifestation of the factorization problem in a somewhat altered context. One resolution is to recast the path integrals as averages

$$\begin{aligned} \overline{\langle \Psi_i | \Psi_j \rangle} &= \delta_{ij}, \\ \overline{\langle \Psi_i | \Psi_j \rangle^2} &= \delta_{ij} + \frac{Z_2}{Z_1^2}, \end{aligned}$$

which are consistent if the quantum amplitude is given by

$$\langle \Psi_i | \Psi_j \rangle = \delta_{ij} + \frac{\sqrt{Z_2}}{Z_1} R_{ij},$$

where  $R_{ij}$  is a random variable with zero mean and unit variance. The conclusion is that the gravitational path integral does not compute exact quantum amplitudes, but quantities averaged over an ensemble of quantum states. This is consistent with the understanding of AdS/CFT in the presence of a wormhole, where the bulk corresponds to an ensemble of quantum theories on the boundaries. Whatever the resolution, the fact that the factorization problem surfaces again in connection with the entropy of black hole radiation is evidence of a deep phenomenon that has yet to be fully understood.

The previous discussion highlights the importance of the path integral in calculating the entropy, but wormholes only contribute significantly to the path integral if they



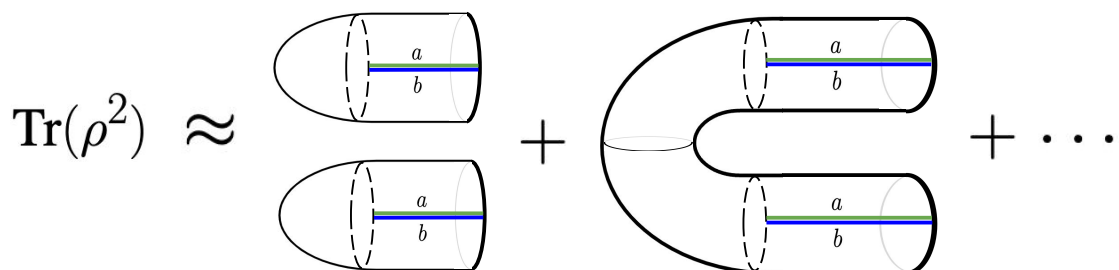


**Figure 8. The purity is computed using replicas of the geometry that are connected in different ways, including connecting the interiors with a wormhole. This figure is adapted from [8].**

are stable, or free of negative modes. Recent work by Marolf and Santos has analyzed the stability of several Euclidean wormhole models in asymptotically anti-de Sitter space [5]. One of the simplest models they analyzed involves three  $U(1)$  gauge fields with two spherical boundaries. This model is closely related to string theory, which permits application of the AdS/CFT correspondence. Specifically, the model is similar to ones generated from string theory when a higher-dimensional space is compactified into lower dimensions. When this happens, additional degrees of freedom are generated. For example, isometries of the internal manifold that is compactified translate into gauge symmetries in the lower-dimensional model, introducing gauge fields like those in the first model studied in [5]. This model captures many important properties of wormholes while remaining analytically and computationally tractable. Marolf and Santos identified a wormhole solution that is free of negative modes, demonstrating that it dominates over the disconnected solution in certain regimes in a manner analogous to the Page transition in the entropy discussed above.

In general, when analyzing the stability of a wormhole solution, it is necessary to consider all the ways the mode can decay, including non-perturbative decay channels. One way a wormhole saddle can decay non-perturbatively is brane nucleation, a phenomenon that occurs in string theory when a true vacuum corresponding to a brane solution has lower energy than the wormhole, as shown in Figure 9 [14]. Because the wormhole is a local minimum, it is perturbatively stable, but quantum fluctuations can produce a bubble of true vacuum that causes the wormhole solution to tunnel to the lower-energy state. Since the  $U(1)^3$  model is an ad-hoc low-energy model, it does not contain branes that can lead to these brane nucleation instabilities, but in a more general setting, these types of decay channels need to be considered.

The goal of this report is to review and reproduce the results of the Euclidean  $U(1)^3$  model of Marolf and Santos, elaborating on the calculations and at times supplying original derivations. Although the model is relatively simple, the perturbative analysis required to determine negative modes does not simply involve diagonalization of a matrix, however computationally intensive that may be when the size of the matrix is large. Instead, because the background is not flat, there is a radial profile that leads to a differential equation that must be solved numerically. Only scalar perturbations were analyzed, but in general, other kinds of perturbations, including vector and tensor perturbations, need to be considered before far-reaching implications for the factorization problem can be made.

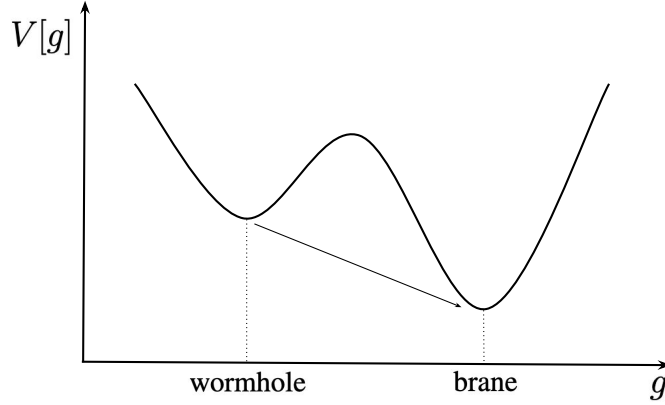


**Figure 9.** A false vacuum corresponding to a wormhole can tunnel through quantum fluctuations into a true vacuum corresponding to a brane solution. In this case, the wormhole is globally unstable even though it is perturbatively stable.

To produce the results discussed in this report, different programs involving several symbolic and numerical tools were written. These programs compute the various tensors, expand the action to second order, and solve the negative mode equation. The results for this model are summarized in this report, but the same kind of analysis and programs can be applied to many different models.

## 2. Einstein-Maxwell Theory with an $S^3$ Boundary

The model consists of three Maxwell fields  $F_{\mu\nu}^i = dA^i$  in four-dimensional AdS space. After introducing the model, Section 2.1 discusses disconnected solutions, and Section 2.2 investigates connected, or wormhole, solutions. Scalar perturbations of the metric around the wormhole solution are discussed in Section 2.3, leading to the eigenvalue problem of Section 2.4 that can be searched for negative modes.

The boundary of AdS is the conformal compactification of Minkowski space in one fewer dimension. In Euclidean signature, this means the boundary of AdS in four dimensions is the three-sphere,  $\partial\mathcal{M} = S^3$ . With this boundary, the action is given by

$$S = - \int_{\mathcal{M}} d^4x \sqrt{g} \left( R + \frac{6}{L^2} - \sum_{i=1}^3 F_{\mu\nu}^i F_i^{\mu\nu} \right) - 2 \int_{\partial\mathcal{M}} d^3x \sqrt{h} K + \mathcal{S}_B, \quad (5)$$

where  $L$  is the AdS length scale,  $h$  is the determinant of the induced metric on  $\partial\mathcal{M}$ , and  $K$  is the extrinsic curvature associated with an outward-pointing normal to  $\partial\mathcal{M}$ . The first integral is called the on-shell Euclidean action. The second term is the Gibbons-Hawking-York term needed to make the variational problem well-defined in the presence of a boundary. The final term, required to make the on-shell action finite, is given by

$$\mathcal{S}_B = \int_{\partial\mathcal{M}} d^3x \sqrt{h} \left( \frac{4}{L} + L\mathcal{R} \right),$$

where  $\mathcal{R}$  is the intrinsic Ricci scalar on  $\partial\mathcal{M}$  [15].

The equations of motion derived by varying Equation 5 with respect to the metric and fields are

$$R_{\mu\nu} + \frac{3}{L^2}g_{\mu\nu} = 2 \sum_{i=1}^3 \left( F_{\mu\rho}^i F_{\nu}^{i,\rho} - \frac{g_{\mu\nu}}{4} F_{\rho\sigma}^i F_i^{\rho\sigma} \right),$$

$$\nabla_\mu F_i^{\mu\nu} = 0.$$

The first equation is the trace-reversed Einstein equations, where the right-hand side is the energy-momentum of the Maxwell fields. The second equation represents the covariant Maxwell equations.

To find solutions, a spherically symmetric metric is used. The metric on the round three-sphere is

$$d\Omega^2 = \frac{1}{4}(\sigma_1^2 + \sigma_2^2 + \sigma_3^2),$$

where  $\sigma_i$ , expressed in terms of Euler angles, are

$$\begin{aligned}\sigma_1 &= -\sin\psi \, d\theta + \cos\psi \sin\theta \, d\varphi, \\ \sigma_2 &= \cos\psi \, d\theta + \sin\psi \sin\theta \, d\varphi, \\ \sigma_3 &= d\psi + \cos\theta \, d\varphi,\end{aligned}$$

with  $\psi \in (0, 4\pi)$ ,  $\theta \in (0, \pi)$ , and  $\varphi \in (0, 2\pi)$ . The full metric takes the form

$$ds^2 = \frac{dr^2}{f(r)} + g(r)d\Omega^2,$$

with  $r \in (0, \infty)$ , where  $r = \infty$  corresponds to the conformal boundary. The vector potentials are given by

$$A^i = L \frac{\sigma_i}{2} \Phi(r).$$

Both disconnected and connected, or wormhole, solutions can be constructed from the metric by appropriate choice of the function  $g$ , which represents the gauge freedom of the metric. The following sections discuss these solutions in detail.

## 2.1. Disconnected Solutions

Disconnected solutions do not involve a connection between asymptotic regions of space-time. Although disconnected solutions do not represent wormholes, it is important to compare them to wormholes to identify which dominates in the path integral. This section investigates disconnected solutions and provides their on-shell Euclidean action, which will be compared later to the action of wormhole solutions.

To find disconnected solutions, the choice  $g(r) = r^2$  is made. At  $r = 0$ , the round three-sphere smoothly shrinks to zero. With this choice, the metric becomes

$$g_{\mu\nu} = \begin{pmatrix} \frac{1}{f(r)} & 0 & 0 & 0 \\ 0 & \frac{1}{4}r^2 & 0 & \frac{1}{4}r^2 \cos\theta \\ 0 & 0 & \frac{1}{4}r^2 & 0 \\ 0 & \frac{1}{4}r^2 \cos\theta & 0 & \frac{1}{4}r^2 \end{pmatrix}.$$

The distinct Einstein equations are

$$2r^4 - L^2 r^3 f'(r) = 2L^4 \left[ r^2 f(r) \Phi'(r)^2 - 4\Phi(r)^2 \right], \quad (6)$$

$$6r^4 - L^2 r^2 \left[ r f'(r) + 4f(r) - 4 \right] = 2L^4 \left[ 4\Phi(r)^2 - r^2 f(r) \Phi'(r)^2 \right]. \quad (7)$$

The Maxwell equations reduce to

$$2r^2 f(r) \Phi''(r) + r^2 \Phi'(r) f'(r) + 2r f(r) \Phi'(r) - 8\Phi(r) = 0. \quad (8)$$

Regularity of the metric and fields requires

$$\begin{aligned} f(0) &= 1, \\ \Phi'(0) &= 0. \end{aligned}$$

With those boundary conditions, the solutions to Equations 6–8 are

$$\begin{aligned} f(r) &= 1 + \frac{r^2}{L^2}, \\ \Phi(r) &= \Phi_0 \frac{\sqrt{L^2 + r^2} - L}{\sqrt{L^2 + r^2} + L}. \end{aligned}$$

It turns out that the energy-momentum tensor is zero, making the disconnected solutions vacuum solutions. The on-shell Euclidean action of the solution evaluates to

$$S_D = 8\pi^2 L^2 (1 + 3\Phi_0^2). \quad (9)$$

## 2.2. Connected Solutions

Using a disconnected metric is one way of solving the equations, but another class of solutions involves a connection between asymptotic regions of spacetime. It is important to identify these solutions because wormholes introduce the factorization problem in AdS/CFT, which is only serious if they dominate over disconnected solutions. It will be shown that this does happen when the source of the Maxwell fields is large enough.

Connected solutions exhibit a wormhole throat with a minimum radius  $r_0$ . To model this, the gauge can be set to  $g(r) = r^2 + r_0^2$ . There are two asymptotic regions, at  $r = \pm\infty$ . A global  $\mathbb{Z}_2$  symmetry relates the two spheres while leaving the minimal sphere invariant.

With the new gauge choice, the unique Maxwell equation is

$$(r^2 + r_0^2) \left[ 2f(r) \Phi''(r) + f'(r) \Phi'(r) \right] + 2r f(r) \Phi'(r) - 8\Phi(r) = 0,$$

which simplifies to

$$\frac{d}{dr} \left[ (r^2 + r_0^2) f(r) \Phi'(r)^2 - 4\Phi(r)^2 \right] = 0.$$

After integration, this becomes

$$f(r) = \frac{C + 4\Phi(r)^2}{(r^2 + r_0^2) \Phi'(r)^2}, \quad (10)$$

where  $C$  is the constant of integration. Using Equation 10, the Einstein equations are

$$\begin{aligned} 2(r^2 + r_0^2)^2 - L^2[(r^2 + r_0^2)rf'(r) + 2r_0^2f(r)] &= 2CL^4, \\ 6(r^2 + r_0^2)^2 - L^2[(r^2 + r_0^2)(rf'(r) + 2f(r) - 4) + 2r^2f(r)] &= -2CL^4. \end{aligned}$$

Combining these two equations yields

$$\Phi'(r)^2 - \frac{L^2r^2[C + 4\Phi(r)^2]}{(r^2 + r_0^2)[CL^4 + (r^2 + r_0^2)(L^2 + r^2 + r_0^2)]} = 0. \quad (11)$$

Rearranging, and again using Equation 10, results in

$$f(r) = \frac{CL^4 + (r^2 + r_0^2)(L^2 + r^2 + r_0^2)}{L^2r^2}. \quad (12)$$

To avoid a singularity at  $r = 0$ , the integration constant must be

$$C = -\frac{L^2r_0^2 + r_0^4}{L^4}.$$

With this choice, Equation 12 becomes

$$f(r) = \frac{L^2 + r^2 + 2r_0^2}{L^2}.$$

From Equation 11, it can be shown that the solution for  $\Phi$  is

$$\Phi(r) = \Phi_* \cosh \left[ \frac{2}{b} F \left( \arctan \left( \frac{r}{La} \right) \middle| 1 - \frac{a^2}{b^2} \right) \right], \quad (13)$$

where  $a \equiv (1 + 16\Phi_*^2)^{1/4}$  and  $b \equiv r_0/L$ . The function  $F(\phi|m)$  is the elliptic integral of the first kind. The elliptic integral parameters are related by

$$b = \sqrt{\frac{a^2 - 1}{2}}.$$

Figure 10 is a plot of  $\Phi(r)$  for  $\Phi_* = 2$  and  $L = 1$ . For some background on elliptic integrals, see Appendix A.2.

The source of the Maxwell fields corresponds to  $\Phi(r)$  at  $r = \infty$ . Taking the  $r = \infty$  limit of Equation 13, the argument of the elliptic integral becomes  $\pi/2$ , reducing it to the complete elliptic integral of the first kind,  $K(m)$ . The source  $\Phi_0$  as a function of  $\Phi_*$  is then

$$\Phi_0(\Phi_*) = \Phi_* \cosh \left[ \frac{2}{b} K \left( 1 - \frac{a^2}{b^2} \right) \right]. \quad (14)$$

For a single value of the source  $\Phi_0$ , there can be two values of  $\Phi_*$ , as shown in Figure 11. Wormhole solutions only exist if  $\Phi_0 \geq \Phi_0^{\min} \approx 3.5633$ , which corresponds to  $\Phi_* = \Phi_*^{\min} \approx 1.0023$ . The different values of  $\Phi_*$  correspond to different wormhole solutions.

Another way of analyzing the two wormhole solutions is by studying how the radius of the wormhole throat changes with the source, as depicted in Figure 12. For

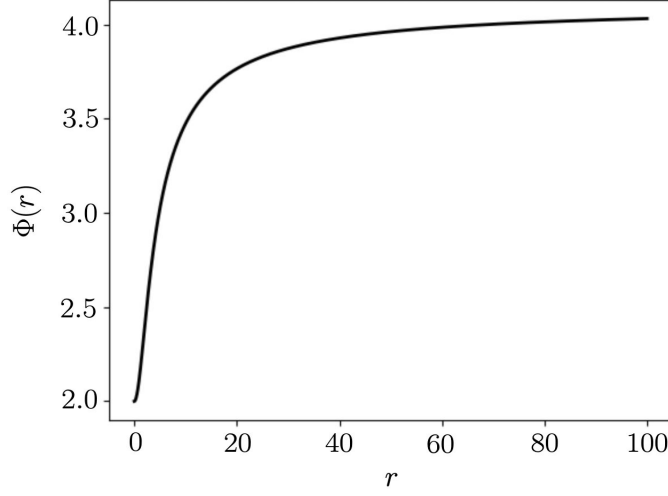


**Figure 10.** Plot of the Maxwell field  $\Phi(r)$  involving the hyperbolic cosine of the elliptic integral of the first kind. The parameters  $\Phi_* = 2$  and  $L = 1$  were used.

$\Phi_0$  above the minimum, there are two values of  $r_0$ , which correspond to small and large wormholes. At  $r_0^{\min} \approx 1.2515L$ , the two wormholes merge. It turns out that only the small wormhole exhibits negative modes.

Substituting the connected wormhole solution into the on-shell Euclidean action of Equation 5, and evaluating the integral, leads to the action

$$S_C = \frac{8\pi^2 L^2}{(X-1)^{3/2}} \left[ 2(X-1)E(-X) - (X-2)K(-X) + \frac{3X}{4\sqrt{X-1}} \sinh \left( 4\sqrt{X-1}K(-X) \right) \right], \quad (15)$$

where  $X \equiv 1 + L^2/r_0^2$  and  $E(m)$  is the complete elliptic integral of the second kind. To assess whether the connected solution has a lower action than the disconnected one, Equation 15 can be subtracted from Equation 9 to produce the metric

$$\Delta S \equiv 2S_D - S_C,$$

which is plotted in Figure 13. The upper and lower branches correspond to the large and small wormhole, respectively. If  $\Delta S > 0$ , the wormhole solution has a lower action, so it should dominate in the path integral. The large wormhole is dominant for  $\Phi_0 \gtrsim 3.8597$ , while the small wormhole is always subdominant. The transition in dominance between the disconnected and large wormhole solutions is analogous to the transition between disconnected and wormhole saddles during black hole evaporation.

### 2.3. Scalar Perturbations

While the large wormhole dominates over the disconnected solution in a certain regime, it is important to know if the wormhole solution is stable. If it is unstable, it can potentially decay into a lower-energy solution, which would have implications for the factorization problem. Determining whether the solution is stable involves identifying negative modes.

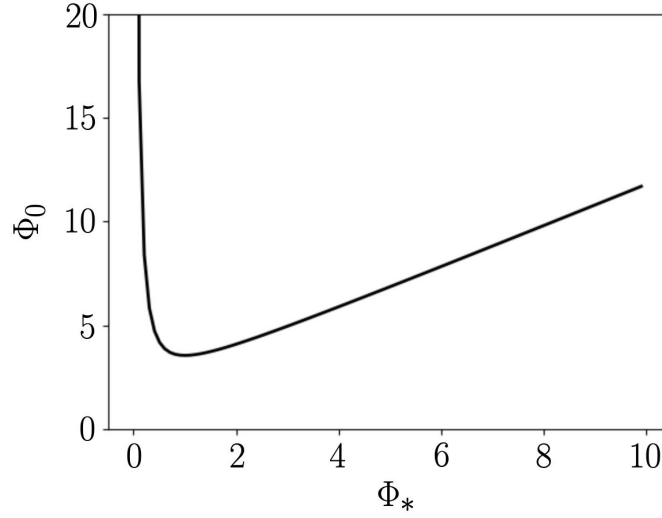


**Figure 11.** The source of the Maxwell fields  $\Phi_0$  as a function of  $\Phi_*$ . There are two types of wormhole solutions for each value of  $\Phi_0$  above the minimum,  $\Phi_0^{\min}$ .

To do this, the metric needs to be perturbed around the wormhole solution. There are several types of perturbations, including scalar, vector, and tensor perturbations, but this report will only focus on scalar perturbations.

The metric and fields take the same form as before, with perturbations  $\delta g$ ,  $\delta f$ , and  $\delta \Phi$  applied to the background fields as

$$\begin{aligned} g(r) &= \bar{g}(r) + \delta g(r), \\ f(r) &= \bar{f}(r) + \delta f(r), \\ \Phi(r) &= \bar{\Phi}(r) + \delta \Phi(r), \end{aligned}$$

where  $\bar{\Phi}(r)$  is given by Equation 13 and

$$\begin{aligned} \bar{g}(r) &= r^2 + r_0^2, \\ \bar{f}(r) &= \frac{L^2 + r^2 + 2r_0^2}{L^2}. \end{aligned}$$

The action is expanded to second order in the perturbations. Integrating out the angular part, the Euclidean on-shell action is

$$S_E = \frac{\pi^2}{8L^2} \int \frac{dr}{\sqrt{fg}} \left[ 12L^4 \left( 4\Phi^2 + fg\Phi'^2 \right) + 3L^2 \left( 2fg'' + f'g' - 4 \right) - 12g^2 \right],$$

where, for simplicity, the explicit dependence on  $r$  in the various functions has been

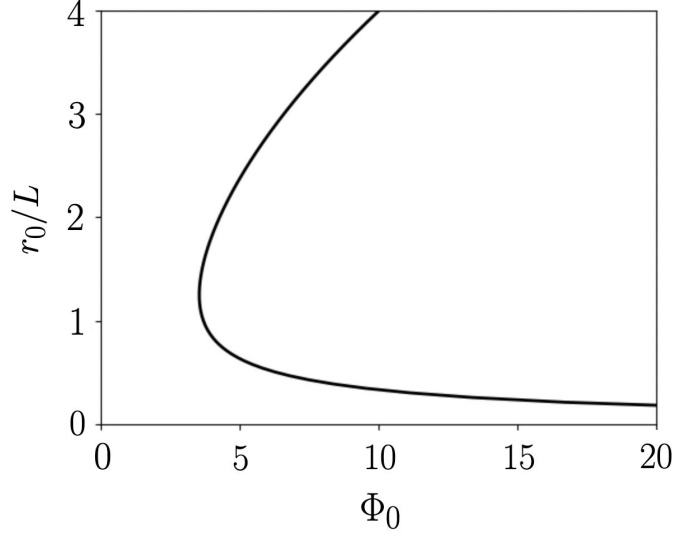


**Figure 12.** The radius of the wormhole throat  $r_0/L$  as a function of  $\Phi_0$ . For  $\Phi_0 \geq \Phi_0^{\min}$ , small and large wormholes exist.

removed. The variations with respect to  $\delta g$  and  $\delta f$ ,

$$\begin{aligned} \frac{\delta S_E}{\delta g} &= -\frac{3\pi^2}{16L^2} \int \frac{dr}{\sqrt{fg^3}} \left[ 12g^2 + 16L^4\Phi^2 + L^2fg'^2 - \right. \\ &\quad \left. 2L^2g(2fg'' + 2fL^2\Phi'^2 + f'g' - 2) \right], \\ \frac{\delta S_E}{\delta f} &= \frac{3\pi^2}{16L^2} \int \frac{dr}{\sqrt{gf^3}} \left[ 4g^2 - 16L^4\Phi^2 - L^2fg'^2 + 4g(L^2 + L^4f\Phi'^2) \right], \end{aligned}$$

vanish because of the Einstein equations. The variation with respect to  $\delta\Phi$  also vanishes because of the unique Maxwell equation

$$\frac{\delta S_E}{\delta\Phi} = -\frac{3L^2\pi^2}{2} \int \frac{dr}{\sqrt{fg}} \left( fg'\Phi' + gf'\Phi' + 2fg\Phi'' - 8\Phi \right).$$

Computing these variations required integrating by parts, producing boundary terms involving  $\delta f$ ,  $\delta g$ , or  $\delta\Phi$ , which go to zero on the boundary. The only non-zero boundary term comes from the variation with respect to  $g$ , which produces a term involving  $\delta g'$ . This term cancels with the variation of the Gibbons-Hawking-York term

$$\delta S_{\text{GHY}} = -2 \int_{\partial\mathcal{M}} d^3x \sqrt{h} \delta K = -6\pi^2 \sqrt{gf} \delta g' \Big|_{\partial\mathcal{M}}.$$

The second-order variation of the action can be decomposed into a part dependent on  $\delta g$  and  $\delta\Phi$  and their derivatives, and a part dependent on  $\delta f$  and its derivative. After integration by parts, the second part has no reliance on  $\delta f'$ . Using Equation 10 to simplify



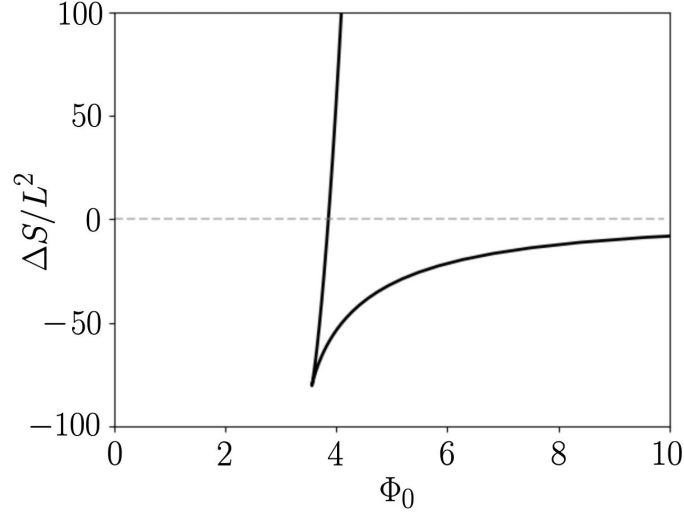


**Figure 13.** The difference in the on-shell Euclidean action between the disconnected and connected wormhole solutions. The upper branch corresponds to the large wormhole, which becomes dominant when  $\Delta S > 0$ , meaning the connected solution has a lower action.

the expression, the  $f$  component of the second-order action is

$$S_f^{(2)} = \frac{\pi^2}{32L^2} \int \frac{dr}{(\bar{g}\bar{f})^{3/2}} \left[ 12L^2\bar{g} \left( L^2\bar{g}\bar{\Phi}'^2 - 3r^2 \right) \delta f^2 - 192L^4\bar{g}\bar{\Phi} \delta f \delta \Phi + \right. \\ \left. 48L^4\bar{f}\bar{g}^2\bar{\Phi}' \delta f \delta \Phi' + 12L^2\bar{g}\bar{f}\bar{g}' \delta f \delta g' - \right. \\ \left. 3 \left( 16L^4\bar{\Phi}^2 + 4L^4\bar{f}\bar{g}\bar{\Phi}'^2 + L^2\bar{f}\bar{g}'^2 + 4L^2\bar{g} + 12\bar{g}^2 \right) \delta f \delta g \right].$$

This action is invariant under the infinitesimal gauge transformation  $\xi \equiv \xi_r(r)\partial_r$ . Under this transformation, a metric perturbation  $h$  and gauge field  $a$  transform as

$$\Delta h = \mathcal{L}_\xi \bar{g},$$

$$\Delta a = \mathcal{L}_\xi \bar{A},$$

where  $\mathcal{L}_\xi$  is the Lie derivative along  $\xi$ , and  $(\bar{g}, \bar{A})$  are the metric and gauge potential background fields. Notice that the  $\bar{g}$  here is different than the  $\bar{g}$  above. From the definition of the Lie derivative, the perturbations transform as

$$\Delta \delta f = \xi_r \bar{f}' - 2\bar{f} \xi_r', \quad (16)$$

$$\Delta \delta g = 2r \xi_r, \quad (17)$$

$$\Delta \delta \Phi = \xi_r \bar{\Phi}'. \quad (18)$$

The transformations of the perturbation derivatives are

$$\Delta \delta g' = 2\xi_r + 2r\xi_r',$$

$$\Delta \delta \Phi' = \xi_r \bar{\Phi}'' + \xi_r' \bar{\Phi}'.$$

Using these transformations, it follows that the gauge transformation of the action  $\Delta S_f^{(2)}$  is zero. Since the action is gauge invariant, it is convenient to choose  $\delta g = 0$ . The action simplifies to

$$S_f^{(2)} = \frac{3\pi^2}{8} \int \frac{dr}{\sqrt{f\bar{g}^3}} \left[ \left( L^2 \bar{g} \bar{\Phi}'^2 - 3r^2 \right) \delta f^2 - L^2 \bar{\Phi} \delta f \delta \Phi + 4L^2 \bar{g}^2 \bar{\Phi}' \delta f \delta \Phi' \right].$$

Given the algebraic dependence on  $\delta f$  in the action, the square can be completed, transforming the action into the form

$$S_f^{(2)} = \int dr \left[ - \left( a_1 \delta f + a_2 \delta \Phi + a_3 \delta \Phi' \right)^2 + C_0 \right],$$

where  $a_i$  are functions of the background fields only. The first term is a Gaussian integral that can be computed, and the result can be absorbed into the measure in the path integral. The remaining part involving  $C_0$  is given by

$$S_f^{(2)} = \frac{\pi^2}{2} \int \frac{dr}{\sqrt{\bar{g}\bar{f}^3} \left( r^2 - L^2 \bar{g} \bar{\Phi}'^2 \right)} \left[ 48L^4 \bar{\Phi}^2 \delta \Phi^2 + 24L^4 \bar{f} \bar{g} \bar{\Phi} \bar{\Phi}' \delta \Phi \delta \Phi' + 3L^4 \left( \bar{f} \bar{g} \bar{\Phi}' \right)^2 \delta \Phi'^2 \right].$$

The part of the action not involving  $f$  can be expressed in terms of the gauge invariant quantity

$$q \equiv \delta \Phi - \bar{\Phi}' \frac{\delta g}{2r}.$$

Using Equations 16–18, it can be shown that  $\Delta q = 0$ . Since this action is also gauge invariant,  $\delta g = 0$  can again be chosen, which means  $q = \delta \Phi$ . Making that simplification, the  $q$  part of the action is

$$S_q^{(2)} = \frac{3L^2\pi^2}{2} \int \frac{dr}{\sqrt{\bar{g}\bar{f}}} \left( 4q^2 + \bar{f}\bar{g}q'^2 \right).$$

The two parts of the action can be combined. After performing integration by parts on the  $qq'$  term in  $S_f^{(2)}$ , the result is

$$S^{(2)} = \frac{\pi^2}{4} \int dr \sqrt{\frac{\bar{g}}{\bar{f}}} \left( \bar{f} K q'^2 + V q^2 \right), \quad (19)$$

where

$$K \equiv \frac{6L^2 r^2}{r^2 - L^2 \bar{g} \bar{\Phi}'^2},$$

$$V \equiv \frac{4K}{\bar{g}} \left[ \frac{2\bar{g}}{L^2 r \bar{f}} \frac{L^2 \left( r - L^2 \bar{\Phi} \bar{\Phi}' \right) + \bar{g} \left( r - 2L^2 \bar{\Phi} \bar{\Phi}' \right)}{r^2 - L^2 \bar{g} \bar{\Phi}'^2} - 1 \right].$$

It is important to note what role the boundary terms of Equation 5 played in deriving this result. As noted earlier, the first-order variation of the Gibbons-Hawking-York term cancels with another boundary term generated when integrating by parts. It can also be shown that the second-order variation is zero. To calculate the contribution the counterterms have, first note that the variation of  $S_B$  is gauge invariant, because it involves fields on the boundary which are invariant under a diffeomorphism in the  $r$  direction. Because the variation of these terms only depends on the variation of  $g$ , making the gauge choice  $\delta g = 0$  drives it to zero. In this way, Equation 19 is the correct form of the second-order action when incorporating all the relevant boundary terms.

## 2.4. Negative Modes

With the action expanded to second order around the wormhole solution, negative modes can be identified by checking if it admits negative eigenvalues. If a solution has a negative eigenvalue, perturbing it will lower the action, which means the perturbations will contribute more in the path integral than the wormhole solution. It will be shown that while negative modes exist, they only occur for the small wormhole solution, which is always subdominant. The large wormhole, which can dominate over disconnected solutions, is free of negative modes.

To search for negative modes, the first term in Equation 19 needs to be integrated by parts, resulting in

$$S^{(2)} = \frac{\pi^2}{4} \int dr \sqrt{\frac{\bar{g}}{\bar{f}}} q \left[ -\sqrt{\frac{\bar{f}}{\bar{g}}} \left( \sqrt{\bar{f} \bar{g}} K q' \right)' + V q \right].$$

The negative mode equation is then

$$-\sqrt{\frac{\bar{f}}{\bar{g}}} \left( \sqrt{\bar{f} \bar{g}} K q' \right)' + V q = \lambda q. \quad (20)$$

If this admits non-trivial solutions for  $\lambda < 0$ , the wormhole solution is locally unstable. Since  $V(r)$  is symmetric around  $r = 0$ , modes can be decomposed into ones where  $q(0) = 0$ , and others where  $q'(0) = 0$ . Equation 20 can be solved numerically given these boundary conditions. Since  $r$  has an infinite range, it is convenient for numerical calculations to switch to a variable with a finite range, introducing

$$r = \frac{r_0 y}{1 - y},$$

so that the conformal boundary lies at  $y = 1$  and the origin at  $y = 0$ . Expanding the derivative in Equation 20 and changing variables, the negative mode equation becomes

$$-K \bar{f} \frac{d^2 y}{dr^2} q''(y) - \left( \bar{f} \frac{dK}{dr} + \frac{r K \bar{f}}{\bar{g}} + \frac{r K}{L^2} \right) \frac{dy}{dr} q'(y) + V(r) q(y) = \lambda q(y). \quad (21)$$

The negative mode equation can be solved numerically by discretizing it and solving the resulting matrix equation using different methods, including QZ factorization and Newton-Raphson search [16; 17]. Discretization involves choosing points on the domain,

and approximating the derivatives at those points using an interpolation function. This reduces differentiation to a matrix operation

$$q'_i \approx D_{ij}q_j.$$

There are several discretization schemes that differ in their choice of grid and interpolation function. The Chebyshev method is a popular method that reduces potentially large oscillations in the interpolated function by sampling points more densely near the edges. This method was used to sample 50 points along the  $y$  axis from 0 to 0.99, which excludes the singularity at  $y = 1$ . See Appendix A.3 for an evaluation of the numerical accuracy.

After discretization, Equation 21 takes the form  $A_{ij}q_j = \lambda Bq_i$ , which is the form of the generalized eigenvalue problem that can be solved using matrix factorization. To incorporate the boundary conditions, the last rows of  $A$  and  $B$  can be modified to reproduce the corresponding equations, either  $q(0) = 0$  or  $q'(0) = 0$ . In both cases, this involves replacing the last row of  $B$  with zeros, since the boundary conditions do not involve  $\lambda$ . For  $q(0) = 0$ , the last row of  $A$  should be one at  $y = 0$  and zero otherwise. For  $q'(0) = 0$ , the last row must be replaced by the row of  $D_{ij}$  corresponding to  $y = 0$ .

To determine whether the small or large wormholes exhibit negative modes, the eigenvalue problem can be solved for different values of the wormhole throat  $r_0$ . Since  $\Phi(r)$  depends on  $r_0$  through  $b$ , adjusting  $r_0$  results in different  $A$  matrices and different eigenvalues. Table 1 summarizes the results for the case  $q'(0) = 0$ . When  $r_0$  is less than  $r_0^{\min}$ , which corresponds to the small wormhole, there is one negative mode. As the wormhole becomes large, the negative mode disappears. Due to the numerical instability of the problem, these results were sensitive to the matrix entries, but the general trend of negative modes for the small wormhole, and positive modes for the large wormhole, was observed. When  $q(0) = 0$ , no negative modes were detected for any value of  $r_0$ .

$r_0/r_0^{\min}$	Eigenvalues
0.8	One negative eigenvalue, $\lambda = -118$
1.0	No negative eigenvalues, $\lambda_{\min} = 1.92 \times 10^{-7}$
1.1	No negative eigenvalues, $\lambda_{\min} = 1.41 \times 10^{-6}$

**Table 1. The eigenvalues of the second-order action around the wormhole solution when  $q'(0) = 0$ . There is one negative mode when the wormhole throat is less than  $r_0^{\min}$ , which becomes positive when  $r_0^{\min}$  is exceeded.**

### 3. Conclusion

Wormholes are important solutions to general relativity that connect distant asymptotic regions of spacetime. There are many different types of wormhole solutions, but they are generally classified as Lorentzian or Euclidean, depending on the signature of the metric. While Lorentzian wormholes may physically connect different parts of the universe, Euclidean wormholes primarily emerge as saddles of the Euclidean gravitational path integral. While these types of wormholes have been studied for decades, they have received renewed interest because they challenge the traditional understanding of the AdS/CFT correspondence and because of their role in resolving the black hole information paradox. Many different types of Euclidean wormholes have been identified, but they only make

significant contributions to the underlying physics if they do not contain negative modes. This report focused on examining wormhole solutions and their negative modes.

Following [5], it was shown that a gravitational theory containing three Maxwell fields has small and large wormhole solutions. The large wormhole solution has a lower Euclidean action than the disconnected one when the source of the Maxwell fields exceeds a critical value. The transition between the disconnected solution and the wormhole mimics the phase transition witnessed between the disconnected and wormhole saddles when computing the entropy of black hole radiation. By conducting a perturbative analysis around the wormhole solution and solving the resulting eigenvalue problem numerically, both negative and positive modes were detected, but the large wormhole did not exhibit negative modes. This indicates that, at least in this simple model, the large wormhole may dominate the path integral, violating factorizability and suggesting that there may be correlations in the dual quantum field theories on the boundaries. This conclusion is based only on analyzing scalar perturbations, but in general, vector- and tensor-based perturbations also need to be considered.

While the model investigated here is illuminating, no definitive conclusions about the AdS/CFT correspondence can be based on it. This is because the AdS/CFT correspondence is a relation involving string theories, but the current model does not embed directly into string theory. For models based on string and M-theory compactifications, non-perturbative decay channels like brane nucleation instabilities need to be considered. Marolf and Santos showed that wormholes in these models that are large enough to dominate over disconnected solutions always suffer from these instabilities. They also identified wormholes that are free of both perturbative and non-perturbative instabilities, but they do not dominate over disconnected solutions.

While subdominant wormholes do not control leading-order effects, they are still important for computing quantities like  $\delta Z^2 \equiv \langle Z^2 \rangle - \langle Z \rangle^2$  that measure the loss of factorizability in the path integral. This is because the contribution of disconnected solutions to this quantity is zero. Unless some mechanism exists that drives  $\delta Z^2$  to zero, even subdominant saddles will make it assume a non-zero value. As [5] concluded, this means that the factorization problem of AdS/CFT is far from resolved and will be the subject of much future research.

## A. Appendix

This appendix provides additional details and references related to the software written to produce the results, and background on needed mathematical methods.

### A.1. Code

While the model examined in this report is relatively simple and for the most part analytically tractable, conducting all the calculations by hand is very time-consuming, error-prone, and does not extend easily to other models. The second-order negative mode equation involving complicated functions of the radial coordinate also needs to be solved numerically. For these reasons, programmatic ways of manipulating symbolic equations and solving them numerically need to be relied on. One major contribution of this report was the creation of Python and Mathematica programs to perform the extensive calculations needed to identify and study wormhole solutions in physically interesting settings.

Several packages were used to produce the results. In Python, `sympy` was used for symbolic computation, including tensor algebra [18]. This package essentially functions as a computer algebra system similar to languages like Mathematica. Calculations of the Ricci tensor and scalar were performed using `einsteinpy` [19]. Jupyter notebooks were used to run and analyze the results [20]. Mathematica was relied on primarily for computing variational derivatives of the action using `VariationalMethods`, which Python cannot do easily. The code can be found in [21], which can be run by following the instructions in the `README`. The relevant notebooks include

- `einstein_maxwell_ads4_euclidean`. Calculates all the quantities in the Einstein and Maxwell equations and verifies the disconnected solution
- `einstein_maxwell_ads4_euclidean_connected`. Verifies the connected wormhole solution
- `einstein_maxwell_ads4_scalar_perturb`. Calculates the variation of the on-shell action
- `second_order_action_analysis`. Calculates the form of the second-order action
- `gauge_invariance_action`. Demonstrates the gauge invariance of the second-order action
- `negative_modes_analysis`. Demonstrates the negative modes for the small wormhole and lack of negative modes for the large wormhole
- `perturbations`. Calculates the first-order variational derivatives of the action to corroborate calculation of the second-order action elsewhere.

The remainder of this section provides code snippets that perform some common calculations using the various packages.

### A.1.1. General Relativity Calculations

Listing 1 is an example of computing tensors needed in general relativity. After defining the required symbolic variables on lines 6–9, the metric is defined on lines 12–17. In this example, the disconnected form of the metric is used, but the connected metric can be defined the same way. On lines 20–22, the Ricci and Einstein tensors are calculated.

```

1 # import packages
2 import sympy
3 from einsteinpy.symbolic import RicciTensor, RicciScalar, MetricTensor,
   ChristoffelSymbols
4
5 # define variables
6 syms = sympy.symbols("r psi theta phi")
7 r, psi, theta, phi = syms
8 f = sympy.Function("f")(r) # metric ansatz
9 L = sympy.symbols("L") # AdS length scale
10
11 # define metric tensor
12 list2d = [[0 for i in range(4)] for i in range(4)]
13 list2d[0][0] = 1 / f
14 list2d[1][1] = list2d[2][2] = list2d[3][3] = r ** 2 / 4
15 list2d[1][3] = list2d[3][1] = r ** 2 / 4 * sympy.cos(theta)

```

```

16 sch = MetricTensor(list2d, syms)
17 metric_array = sympy.MutableDenseNDimArray(list2d)
18
19 # compute Ricci and Einstein tensors
20 Ric = RicciTensor.from_metric(sch)
21 einstein_tensor = sympy.MutableDenseNDimArray(Ric.tensor()) + 3 / L **
    2 * metric_array
22 einstein_tensor = sympy.simplify(einstein_tensor)

```

**Listing 1. Example of computing the Ricci and Einstein tensors symbolically using `einsteinpy`.**

### A.1.2. Tensor Algebra Calculations

Often in general relativity calculations, it is necessary to contract tensor indices. Listing 2 is an example of computing the energy-momentum tensor of a Maxwell field, which involves various contractions. Note that this example is not self-contained, but uses some variables defined in Listing 1. After defining the vector potential on line 6, lines 9–19 compute the field strength tensor. Using `sympy`, lines 22–28 compute the first term in the energy-momentum tensor involving a single contraction. The object `TensorHead` is used to perform the contraction. Lines 31–34 do the same for the second term, and the final result is computed on line 37.

```

1 # import packages
2 from sympy.tensor.tensor import TensorIndexType, TensorIndex,
    TensorHead, tensor_indices, TensorSymmetry
3
4 # define vector potential
5 cap_phi = sympy.Function("Phi")(r) # defines gauge field
6 A = L / 2 * cap_phi * sympy.Array([0, 0, -sympy.sin(psi), sympy.cos(psi)
    ] * sympy.sin(theta))
7
8 # compute field strength tensors
9 x = [r, psi, theta, phi]
10
11 def em_field_strength(A):
12     """Compute EM field strength from the vector potential."""
13     F = sympy.MutableDenseNDimArray.zeros(4, 4)
14     for i in range(4):
15         for j in range(4):
16             F[i, j] = sympy.diff(A[j], x[i]) - sympy.diff(A[i], x[j])
17     return F
18
19 F = em_field_strength(A)
20
21 # compute first term of energy-momentum tensor involving single
    contraction
22 metric_inv = sympy.Matrix(metric_array).inv()
23 Euclidean = TensorIndexType("Euclidean", dummy_name="E")
24 i0, i1, i2, i3, i4, i5, i6, i7 = tensor_indices("i0:8", Euclidean)
25 FFg_tensor = TensorHead("FFg", [Euclidean] * 6)
26 FFg_matrix = sympy.tensorproduct(F, F, metric_inv)
27 repl = {FFg_tensor(-i0, -i1, -i2, -i3, i4, i5): FFg_matrix}

```

```

28 T_contracted_1 = FFgg_tensor(-i0, -i1, -i2, -i3, i3, i1).
    replace_with_arrays(repl)
29
30 # compute second term of energy-momentum tensor involving two
    contractions
31 FFgg_tensor = TensorHead("FFgg", [Euclidean] * 8)
32 FFgg_matrix = sympy.tensorproduct(F, F, metric_inv, metric_inv)
33 repl = {FFgg_tensor(-i0, -i1, -i2, -i3, i4, i5, i6, i7): FFgg_matrix}
34 T_contracted_2 = FFgg_tensor(-i0, -i1, -i2, -i3, i3, i1, i2, i0).
    replace_with_arrays(repl)
35
36 # compute energy-momentum tensor
37 energy_momentum = 2 * (T_contracted_1 - metric_array / 4 *
    T_contracted_2)

```

**Listing 2. Example of calculating the energy-momentum tensor of a Maxwell field using sympy.**

## A.2. Elliptic Integrals

Elliptic integrals historically arose in the context of finding the arc length of an ellipse [22]. They can be applied to many areas of physics, including determining the motion of a simple pendulum or the deflection of a thin elastic bar. An elliptic integral is an integral of the form

$$\int \frac{A(x) + B(x)}{C(x) + D(x)\sqrt{S(x)}} dx,$$

where  $A$ ,  $B$ ,  $C$ , and  $D$  are polynomials in  $x$  and  $S$  is a polynomial of degree three or four.

Elliptic integrals come in three different kinds. The incomplete elliptic integral of the first kind is given by

$$F(\phi|m) \equiv \int_0^\phi \frac{d\theta}{\sqrt{1 - m^2 \sin^2 \theta}}.$$

The parameter  $\phi$  is called the amplitude, and  $m$  the modulus. The complete integral of the first kind is obtained by setting  $\phi = \pi/2$ ,  $K(m) \equiv F(\pi/2, m)$ . The incomplete elliptic integral of the second kind is given by

$$E(\phi|m) \equiv \int_0^\phi \sqrt{1 - m^2 \sin^2 \theta} d\theta.$$

As before, the complete version is  $E(m) \equiv E(\pi/2, m)$ . The third kind is written similarly to the first two, but it is not used in this report and will not be reviewed.

## A.3. Chebyshev Differentiation

To solve a differential equation numerically, the function and its derivatives need to be discretized. There are different ways of choosing discretization points and interpolating between them to approximate the derivatives. One of the simplest discretization methods is finite differencing. An example of this method is second-order central differencing, which produces the first and second derivatives at the discretization points

$$f'_i = \frac{f_{i+1} - f_{i-1}}{2\Delta x},$$

$$f''_i = \frac{f_{i+1} - 2f_i + f_{i-1}}{\Delta x^2},$$



where  $\Delta x$  is the spacing between the points. Another popular method is Chebyshev differentiation. By using unevenly spaced points, it mitigates potentially large errors that occur near the edges of the domain. The discretization points are

$$x_i = \frac{1}{2}(x_{\min} + x_{\max}) + \frac{1}{2}(x_{\max} - x_{\min}) \cos\left(\frac{i\pi}{N}\right), \quad i = 0, 1, \dots, N,$$

where  $x_{\min}$  and  $x_{\max}$  define the minimum and maximum of the domain, respectively. The differentiation matrix is given by

$$D_{ij} = \begin{cases} \sum_{k \neq i} \frac{1}{x_i - x_k}, & i = j \\ \frac{a_i}{a_j(x_i - x_j)}, & i \neq j \end{cases}$$

where

$$a_i = \prod_{j \neq i} (x_i - x_j).$$

Figure 14 shows the result of applying Chebyshev differentiation to approximate the first and second derivatives of  $u(x) = e^x \sin 5x$ . The blue points are the estimated derivatives at the sampled points, while the black curves are the true derivatives. When  $N = 10$  points are used, the estimates generally track the true values, but there can be large errors. With  $N = 50$  points, the reconstruction error is very small. Notice that the functions are sampled more densely near the edges.

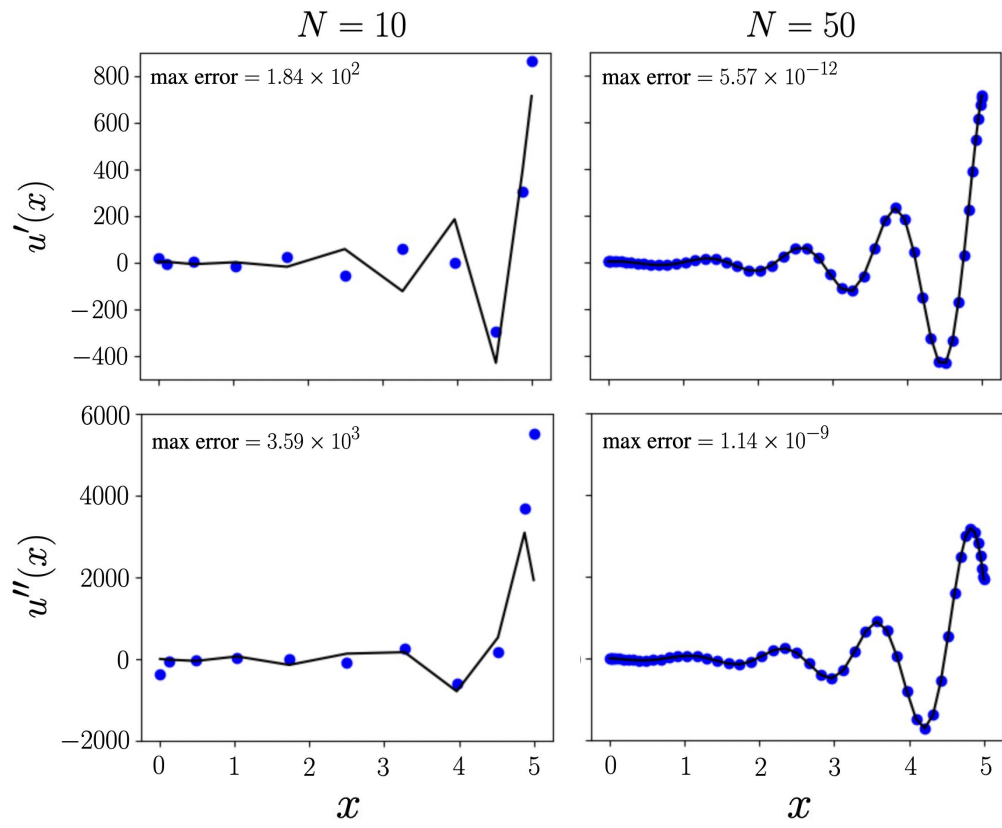


**Figure 14. Chebyshev differentiation of  $u(x) = e^x \sin 5x$  using different amounts of discretization points. When  $N = 10$ , the maximum estimation error of  $u'$  and  $u''$  is large, but when  $N = 50$ , the error becomes very low.**

## References

- [1] A. Kundu, “Wormholes and Holography: An Introduction,” *The European Physical Journal C*, vol. 82, no. 5, may 2022. [Online]. Available: <https://doi.org/10.1140%2Fepjc%2Fs10052-022-10376-z>
- [2] J. Maldacena, “The Large N Limit of Superconformal Field Theories and Supergravity,” *International Journal of Theoretical Physics*, vol. 38, no. 4, pp. 1113–1133, 1999. [Online]. Available: <https://doi.org/10.1023%2Fa%3A1026654312961>
- [3] E. Witten, “Anti De Sitter Space and Holography,” 1998. [Online]. Available: <https://arxiv.org/abs/hep-th/9802150>
- [4] J. Maldacena and L. Maoz, “Wormholes in AdS,” *Journal of High Energy Physics*, vol. 2004, no. 02, pp. 053–053, feb 2004. [Online]. Available: <https://doi.org/10.1088%2F1126-6708%2F2004%2F02%2F053>
- [5] D. Marolf and J. E. Santos, “AdS Euclidean Wormholes,” *Classical and Quantum Gravity*, vol. 38, no. 22, p. 224002, oct 2021. [Online]. Available: <https://doi.org/10.1088%2F1361-6382%2Fac2cb7>
- [6] J. Cotler and K. Jensen, “Gravitational Constrained Instantons,” *Physical Review D*, vol. 104, no. 8, oct 2021. [Online]. Available: <https://doi.org/10.1103%2Fphysrevd.104.1081501>
- [7] D. N. Page, “Information in Black Hole Radiation,” *Physical Review Letters*, vol. 71, no. 23, pp. 3743–3746, dec 1993. [Online]. Available: <https://doi.org/10.1103%2Fphysrevlett.71.3743>
- [8] A. Almheiri, T. Hartman, J. Maldacena, E. Shaghoulian, and A. Tajdini, “The Entropy of Hawking Radiation,” *Reviews of Modern Physics*, vol. 93, no. 3, jul 2021. [Online]. Available: <https://doi.org/10.1103%2Frevmodphys.93.035002>
- [9] S. Ryu and T. Takayanagi, “Holographic Derivation of Entanglement Entropy from the anti-de Sitter Space/Conformal Field Theory Correspondence,” *Physical Review Letters*, vol. 96, no. 18, may 2006. [Online]. Available: <https://doi.org/10.1103%2Fphysrevlett.96.181602>
- [10] J. D. Bekenstein, “Black Holes and Entropy,” *Phys. Rev. D*, vol. 7, pp. 2333–2346, Apr 1973. [Online]. Available: <https://link.aps.org/doi/10.1103/PhysRevD.7.2333>
- [11] N. Engelhardt and A. C. Wall, “Quantum Extremal Surfaces: Holographic Entanglement Entropy beyond the Classical Regime,” *Journal of High Energy Physics*, vol. 2015, no. 1, jan 2015. [Online]. Available: <https://doi.org/10.1007%2Fjhep01%282015%29073>
- [12] A. Almheiri, T. Hartman, J. Maldacena, E. Shaghoulian, and A. Tajdini, “Replica Wormholes and the Entropy of Hawking Radiation,” *Journal of High Energy Physics*, vol. 2020, no. 5, may 2020. [Online]. Available: <https://doi.org/10.1007%2Fjhep05%282020%29013>
- [13] G. Penington, S. H. Shenker, D. Stanford, and Z. Yang, “Replica Wormholes and the Black Hole Interior,” 2019. [Online]. Available: <https://arxiv.org/abs/1911.11977>
- [14] S.-H. H. Tye, D. Wohns, and Y. Zhang, “Coleman–de Luccia Tunneling and the Gibbons–Hawking Temperature,” *International Journal of Modern Physics A*, vol. 25, no. 05, pp. 1019–1060, feb 2010. [Online]. Available: <https://doi.org/10.1142%2Fs0217751x10047981>
- [15] K. Skenderis, “Lecture Notes on Holographic Renormalization,” *Classical and Quantum Gravity*, vol. 19, no. 22, pp. 5849–5876, nov 2002. [Online]. Available: <https://doi.org/10.1088%2F0264-9381%2F19%2F22%2F306>

- [16] Ó. J. C. Dias, J. E. Santos, and B. Way, “Numerical Methods for Finding Stationary Gravitational Solutions,” *Classical and Quantum Gravity*, vol. 33, no. 13, p. 133001, jun 2016. [Online]. Available: <https://doi.org/10.1088/0264-9381/33/13/133001>
- [17] L. N. Trefethen, *Spectral Methods in MATLAB*. Society for Industrial and Applied Mathematics, 2000.
- [18] A. Meurer, C. P. Smith, M. Paprocki, O. Čertík, S. B. Kirpichev, M. Rocklin, A. Kumar, S. Ivanov, J. K. Moore, S. Singh, T. Rathnayake, S. Vig, B. E. Granger, R. P. Muller, F. Bonazzi, H. Gupta, S. Vats, F. Johansson, F. Pedregosa, M. J. Curry, A. R. Terrel, v. Roučka, A. Saboo, I. Fernando, S. Kulal, R. Cimrman, and A. Scopatz, “SymPy: Symbolic Computing in Python,” *PeerJ Computer Science*, vol. 3, p. e103, Jan. 2017. [Online]. Available: <https://doi.org/10.7717/peerj-cs.103>
- [19] EinsteinPy Development Team, *EinsteinPy: Python Library for General Relativity*, 2021. [Online]. Available: <https://einsteinpy.org/>
- [20] T. Kluyver, B. Ragan-Kelley, F. Pérez, B. Granger, M. Bussonnier, J. Frederic, K. Kelley, J. Hamrick, J. Grout, S. Corlay, P. Ivanov, D. Avila, S. Abdalla, and C. Willing, “Jupyter Notebooks – A Publishing Format for Reproducible Computational Workflows.”
- [21] J. Chryssathacopoulos. (2022) Analysis of Wormholes using Python. [Online]. Available: <https://github.com/jchryssanthacopoulos/wormholes>
- [22] J. R. Culham. Elliptic Integrals, Elliptic Functions and Theta functions. [Online]. Available: [http://www.mhtlab.uwaterloo.ca/courses/me755/web\\_chap3.pdf](http://www.mhtlab.uwaterloo.ca/courses/me755/web_chap3.pdf)